Springer

KSME

Analysis of the wheel/rail rolling contact fatigue of a high-speed train under the transient mechanism[†]

Qian Xiao[1,2,*], Jifeng Zheng[1], Jihua Liu[1] and Jun Fang[1]

[1] *Modern Railway Vehicle Institute, East China Jiaotong University, Nanchang, 330013, China*
[2]*State Key Laboratory of Traction Power, Southwest Jiaotong University, Chengdu, 610031, China*

Abstract

The Rolling contact fatigue (RCF) damage of high-speed wheels is a main factor that affects railway safety. This paper presents a Finite element model (FEM) of high-speed transient rolling contact that considers kinetic parameters as initial conditions. This model is used to calculate wheel/rail RCF. With a CRH2 high-speed train as the research object, a head car model is established with the multibody dynamics software UM. The train is driven on a straight track at a speed of 300 km/h. Different contact geometric parameters, such as lateral displacement and attack angle, are obtained. A 3D high-speed transient elastic-plastic FEM of wheel/rail rolling contact is then developed by using ABAQUS with the initial dynamic contact geometric parameters. The actual geometries of the wheel tread and rail head as well as the elastic-plastic properties are considered in this model. This consideration makes the model highly suitable for solving 3D transient rolling contact behavior. The normal force, creep force, and contact area in the contact patch are solved and used in the fatigue model. Owing to the hunting movement of wheels, the wheel/rail force and lateral displacement change significantly at 0.2 and 0.5 s. The longitudinal and lateral creep force increase sharply with the increase in shear stress. The work states of the wheel/rail at 0.2 and 0.5 s easily reach the ratchet effect zone, and the fatigue index is large. The fatigue damage of the wheels is generally near the nominal rolling circle.

Keywords: Wheel/rail relationship; Rolling contact fatigue; Transient contact characteristics; High-speed train

---

1. Introduction

With the increase in the axle loads and speeds of railway vehicles, the Rolling contact fatigue (RCF) damage of wheels has become the main factor that influences wheel life and transport safety. To improve the dynamic performance of vehicles and reduce the fatigue damage of wheels/rails, domestic and foreign scholars have conducted a significant amount of research. A plane-strain Finite element model (FEM) of rails was established by Deng t al. by using the finite element analysis software ABAQUS. The repeated rolling of wheels on rails was simulated with moving load. Fatigue crack initiation life was calculated with Jiang's fatigue model, and the effects of rail material defect (hole) and friction coefficient on fatigue crack initiation life were analyzed [1]. Hertz theory and the finite element software ANSYS were used by Cao et al. to analyze the contact fatigue problem of wheels/rails with surface cracks. Under the condition of different axle loads and operating states, the stress intensity factors of crack tips at different locations were obtained. The finite element

method is an effective method to solve the complex contact fatigue problem of wheels/rails because Hertz theory does not consider the plasticity of materials and the friction between wheels and rails [2]. The law of surface crack initiation of wheel treads was analyzed by Taraf et al. by using a 2D elastic-plastic FEM of wheel/rail rolling contact with mobile Hertz contact pressure. This work proved that material defects, axle load, and the friction coefficient directly affect the RCF damage of wheels/rails [3]. Lee [4] studied the influence of creep rate on RCF crack initiation life by establishing a 3D finite element static model that considers tangential traction force. The RCF damage coefficient of rails was measured by Ding [5] with an abrasion-damage function to obtain the fatigue damage distribution and characteristics of rails in actual lines. Generally, these results on the RCF of wheels/rails were solved with 2D or 3D steady-state FEMs.

However, the initial conditions of these models were confirmed during the entire computing process. Meanwhile, the rolling contact state of wheels/rails is difficult to simulate accurately and effectively. The rapid development of computers and finite element software in recent years has facilitated the simulation of transient wheel/rail rolling contact in
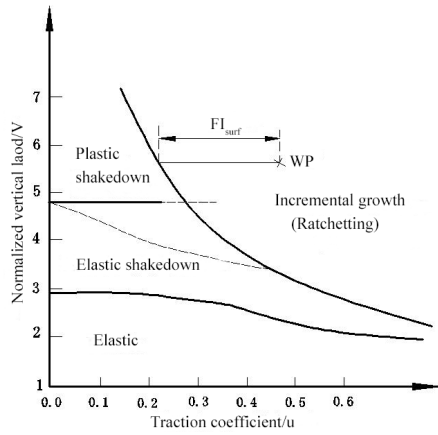

Fig. 1. Shakedown map.

consideration of real geometry [6-9]. However, only a few studies explored wheel/rail RCF.

The present work employed a 3D transient rolling contact FEM to solve the RCF of high-speed wheels/rails in the time domain. This FEM is valid for rolling speeds of up to 300 km/h. Emphasis was placed on detailed contact solutions. With the numerical results, improved understanding of the mechanism of RCF was achieved.

2. Prediction theory and method of transient RCF

A 3D transient rolling contact model was established by combining implicit and explicit methods to study the high-speed transient rolling contact of wheels/rails. This model can accurately simulate actual wheel/rail contact behaviors. While considering wheel/rail contact parameters, such as longitudinal and lateral creep force, area of the contact patch as the input parameters of the shakedown map [10-12], and the damage function [13-15], this work analyzed the status and fatigue damage distribution of wheels.

2.1 Shakedown map

A shakedown map comprehensively utilizes wheel/rail contact stress and the traction coefficient to evaluate wheel loading capacity (Fig. 1). The Y-axis represents dimensionless contact stress V, and the X-axis represents traction coefficient *u*.

Fig. 1 shows that the shakedown map of the entire area is divided into four subdomains according to the value of *V* and *u*. They are marked as elastic state, elastic shakedown, plastic shakedown, and ratchet effect zone. Plastic shakedown and ratchet effect, which appears in the contact area, primarily contribute to contact fatigue crack initiation on the wheel/rail surface. These two features are the major components of fatigue crack initiation. The work point (WP, wheel/rail contact point) position on the shakedown map was determined with Eqs. (1) and (2). The contact fatigue index (FI$_{surf}$) was obtained according to Eq. (3). With the shakedown map, a qualitative analysis of RCF was performed; in this analysis, the

Table 1. Parameters of wheel RCF damage function.

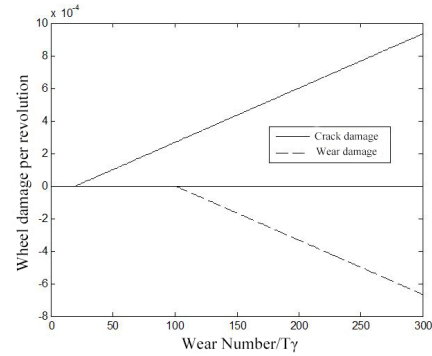| Parameters	Value
Crack initiation value	$20\,N$
Crack propagating rate	$3.6 \times 10^{-6}\,r\,/\,N$
Wear initiation value	$100\,N$
Wear rate	$-5.4 \times 10^{-6}\,r\,/\,N$

Fig. 2. Wheel RCF damage function.

relationship between wear and RCF was disregarded.

$$V = P_0 / K \,,\tag{1}$$

where K is the maximum contact stress (N/m^2) and K is pure shear yield strength (N/m^2).

$$u = \sqrt{F_\xi^2 + F_\eta^2}\Big/F_n \,,\tag{2}$$

where F_ξ is the longitudinal creep force (N) and F_η is the lateral creep force (N).

$$FI_{surf} = u - \frac{2\pi abK}{3F_n} \,,\tag{3}$$

where F_n is contact normal force (N) and a and b are the lengths of the contact ellipse semi-axis (m).

The RCF of high-speed wheels/rails was verified. The WP is on the right side of the ratchet effect curve, that is, FI$_{surf}$> 0.

2.2 Damage function

With the life cycle model, the British Rail Safety and Standards Committee explored further the development of wheel wear and RCF models. The RCF damage function of an integral rolled steel wheel is depicted in Fig. 2 [16, 17], and its damage function parameters are shown in Table 1 [5].

The results of wheel wear and RCF obtained from the field were compared with those obtained from the shakedown map and damage function. The wheel wear and RCF results predicted by these two models were generally consistent with those obtained from the field. The RCF damage function of a wheel, which is based on energy dissipation in the contact
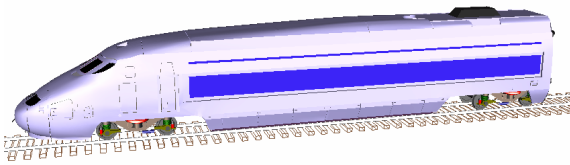
Fig. 3. Parameterized head car model set up in UM.

patch, comprehensively considers the influence of longitudinal and lateral creep force (rate) on wheel RCF as well as the relationship between wear and RCF. The prediction model depends on the value of the wear index (T_γ), which is expressed as

$$T_\gamma = T_\xi \gamma_\xi + T_\eta \gamma_\eta,$$ (4)

where ξ and η are longitudinal and lateral, respectively; T is tangential force (N); and γ is the creep rate.

Serving as the initial conditions, the dynamic contact geometric parameters included wheel/rail contact normal force, creep force (rate), and contact patch area. With these conditions, a 3D transient elastic-plastic FEM of high-speed wheel/rail rolling contact was developed with ABAQUS.

3. Establishment of the RCF calculation system

The FEM of high-speed transient rolling contact based on the initial conditions of kinetic parameters can be used to effectively calculate wheel/rail RCF. A head car model of CRH2 was built with the multibody dynamics software UM. The lateral displacement and contact geometric parameters, such as attack angle during hunting movement, were obtained by simulating a train driven on a straight track at a speed of 300 km/h. With the dynamic contact geometric parameters as the initial conditions, a 3D transient elastic-plastic FEM of high-speed wheel/rail rolling contact was established with the nonlinear finite element software ABAQUS. Finally, the distribution of wheel fatigue damage was analyzed by plotting the maximum von Mises stress, longitudinal creep force, and lateral creep force within the contact patch into the shakedown map and fatigue damage function.

3.1 Establishment of a dynamic model and its validation

With the CRH2 high-speed train as the research object, a head car model of CRH2 was established with the multibody dynamics software UM. This model was simplified into three components, namely, car body, bogie, and wheel set, and each was regarded as rigid. The model consisted of 50 degrees of freedom. Many nonlinearities, such as wheel/rail contact geometry, lateral stop, and primary suspension, were considered. The sixth-grade track irregularity PSD of the U.S. was set as the track irregularity. Table 2 shows the values of the simulation parameters involved in the UM model; these values were all derived from the actual vehicle system of CRH2. The re-

Table 2. Parameters involved in the UM model.

| Parameter		Value
Lateral span between rolling circles		1493 *mm*
Distance between backs of the wheel flanges		1353 *mm*
Wheel profile		LMA
Rail profile		60 *kg / m*
Primary suspension	Longitudinal stiffness of steel spring	980 *kN / m*
	Lateral stiffness of steel spring	980 *kN / m*
	Vertical stiffness of steel spring	1,176 *kN / m*
	Vertical damping	19.6 *kN · s / m*
Secondary suspension	Longitudinal stiffness of air spring	158.76 *kN / m*
	Lateral stiffness of air spring	158.76 *kN / m*
	Vertical stiffness of air spring	189.14 *kN / m*
	Lateral damping	58.8 *kN · s / m*
	Vertical damping	40.0 *kN · s / m*
Anti-yaw damper		2500 *kgf / cm / s*
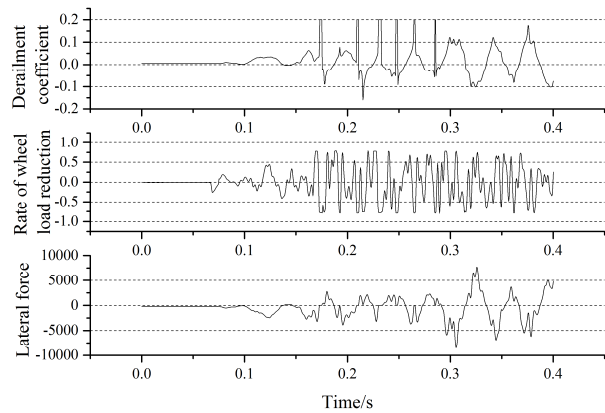
Fig. 4. Curves of derailment coefficient, rate of wheel load reduction, and lateral force varying with time.

sulting model is shown in Fig. 3.

The indices of derailment coefficient, rate of wheel load reduction, and wheel/rail lateral force are generally used to evaluate train operation safety. These three indices were solved in this study to validate the accuracy of the multi-body dynamics model (Fig. 4). According to the high-speed EMU test specification of China [18], the derailment coefficient and rate of wheel load reduction should not exceed 0.8 for a maximum operating speed of 200 km/h (Fig. 4). The data in the figure match the standard values. As indicated in the comparison of the simulation results with those in related literature [19, 20], the orders of magnitude of the indices of derailment coefficient, rate of wheel load reduction, and wheel/rail lateral force are consistent.

Fig. 5 shows the curves of wheel/rail force, lateral displacement, attack angle, and velocity of the left wheel in the former bogie varying with time. The varying values of lateral displacement ranged from 0 mm to 0.005 mm, and those of the attack angle ranged from 0 rad to 0.0015 rad. A hunting

Table 3. Dynamic parameters in different times.

Moment (s)	Wheel/rail force (N)	Transverse displacement (m)	Attack angle (rad)	Speed (m/s)
0.2	74589	-3.5e-4	-9.2e-4	83.3339
0.3	46472	-5.7e-4	-4.1e-4	83.3351
0.4	50680	-2.25e-3	-3.8e-4	83.3321
0.5	53853	-2.51e-3	4.36e-5	83.3290
0.6	26788	-1.13e-3	1.89e-4	83.3286
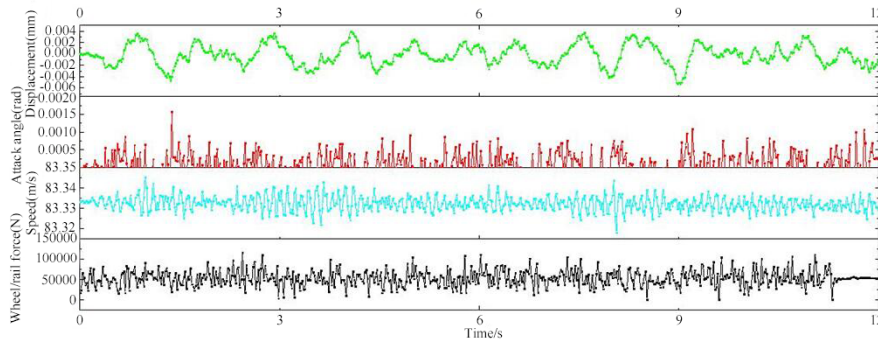
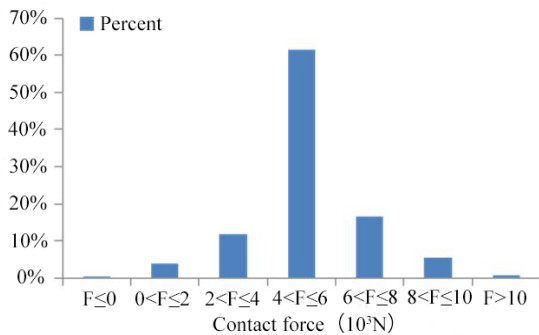Fig. 5. Curves of wheel/rail force, lateral displacement, attack angle, and speed varying with time.

Fig. 6. Distribution of wheel/rail force value within the entire running time.
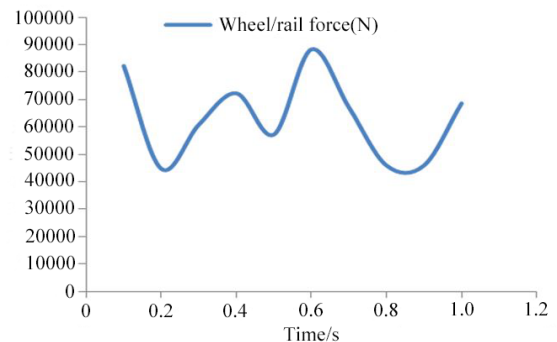

Fig. 7. Wheel/rail force diagram within the entire running time.

movement of a short operation cycle occurred when the train was running at a high speed. Through a statistical analysis of contact force, the distribution within the entire running time was obtained, as shown in Fig. 6. The proportion of wheel/rail force from 20000 N to 80000 N was more than 90 %, and it shared the same regularity within every time interval of 0.1 s. Thus, an interval of 0.1 s is highly suitable for discretizing the wheel/rail force (Fig. 7). The other wheel/rail contact geometric parameters at 0.2, 0.3, 0.4, 0.5 and 0.6 s were also obtained in the same manner.

3.2 Establishment of the FEM

The kinetic parameters at 0.2 s to 0.6 s with an interval of 0.1 s (Table 3) were added to the 3D transient elastic-plastic FEM of wheel/rail rolling contact (Fig. 8). The real wheel/rail geometric profile, elastic-plastic constitutive model of the material, boundary conditions, and functional friction model were utilized.

Eight-node hexahedral solid elements were applied to discretize the wheelset and rail. The element of the solution zone was refined to 1 mm. The wheel profile was an LMA type, and the rail was a standard CHN60 with an inclination of 1:40. The total numbers of elements and nodes were 7.69×10^5 and 7×10^5, respectively. A penalty method based on a surface-to-surface contact algorithm was employed to solve the wheel/rail rolling contact behavior. Coulomb's law of friction was followed in the process.

For the solution, the following boundary conditions were applied. All the displacements of the nodes at the bottom of the rail are holonomic constraints, and the two ends of the rail are symmetric constraints. An axle load of 14 tons was applied to the geometric center of the wheelset. Table 4 shows the values of the simulation parameters involved in the FEM.

Table 4. Parameters involved in the FEM.

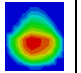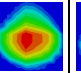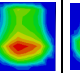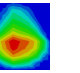| Parameter		Value
Coefficient of friction, f		0.25
Wheel diameter, ϕ		0.86 m
Wheelset mass, M_W		2100 kg
Stiffness of primary suspension, K		980 kN / m
Damping of primary suspension, C		19.6 $kN \cdot s / m$
Wheel/rail material	Young's modulus, E	205 Gpa
	Poisson's ratio, v	0.3
	Density, ρ	7800 kg / m^3
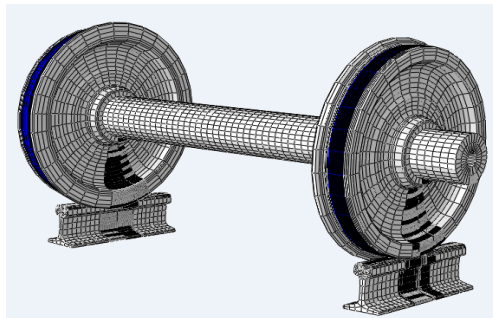
(a) Overall model
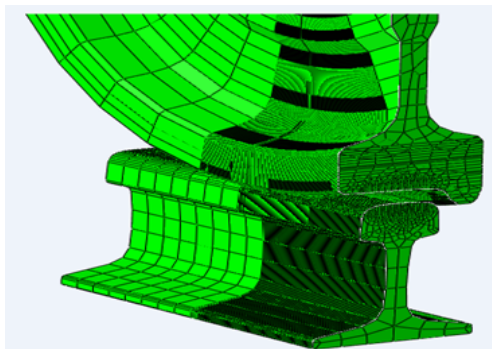
(b) Local model
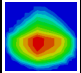
Fig. 8. 3D transient elastic-plastic FEM of high-speed wheel/rail rolling contact.

4. Analysis of numerical calculation results

4.1 Longitudinal, lateral creep force, and contact patch area

The parameters of the wheel/rail contact patch at different moments of a dynamic period were calculated with the transient FEM of rolling contact, as shown in Table 5. The longitudinal creep force at 0.2 s was large because of the large normal force. Furthermore, the normal force and lateral displacement at 0.3 s, as well as the value of longitudinal creep force, were relatively small. Contrary to that at 0.3 s, the large attack angle at 0.2 s led to a large lateral creep force [21]. The contact area was significantly large at 0.5 s because of the emergence of a main contract area and a secondary contact area within the contact patch resulting from large lateral displacement. The distributions of the longitudinal and lateral

Table 5. Parameters of wheel contact patch under different moments.

Moment (s)	0.2	0.3	0.4	0.5	0.6
Maximum longitudinal creep force (N)	16222.5	10245.2	15512.4	11903.6	14013.5
Maximum lateral creep force (N)	985.146	−263.415	695.837	989.623	−859.745
Contact patch area (mm²)	248.46	226.96	235.8	251.06	242.54
Contact patch shape					

creep force under different moments are shown in Figs. 9 and 10, respectively. The distributions of the longitudinal and lateral creep force are almost consistent, except for that at 0.5 s. As a result of the large lateral displacement and change in contact position, two peaks of lateral creep force appeared in different regions at 0.5 s. This condition is due to the existence of rail inclination, which caused compressive stress in the partial contact patch and tensile stress in the other part. The large lateral displacement also contributed to this condition.

4.2 Shakedown map

The variation in the contact patch under high-speed rolling contact was studied with a 3D transient elastic-plastic FEM of high-speed wheel/rail rolling contact. The longitudinal and lateral creep force became steady easily. The contact patch parameters of the shakedown map are shown in Fig. 11. The longitudinal and lateral creep force significantly contributed to the appearance of shear stress, that is, large creep force equates to large shear stress. A wheel with a large shear stress easily reaches the ratchet effect zone. At 0.5 and 0.2 s, the longitudinal and lateral creep force were significantly large; hence, they were prone to RCF. However, at 0.3, 0.4 and 0.6 s, the wheel was in the elastic shakedown zone, which is a relatively safe state.

4.3 RCF damage distribution of the wheel under different moments

The accumulated RCF damage under the kinetic parameters of different moments is illustrated in Fig. 12. As a result of the large wheel/rail creep force and the corresponding increase in shear stress, the wheel tended to enter the ratchet effect zone or plastic shakedown zone, which resulted in fatigue damage of the wheel from 0.2 s to 0.5 s. Almost no damage occurred at 0.6 s. The largest fatigue damage occurred at 0.2 s, and the damage location was near the rolling circle of the wheel. The fatigue damage at 0.3 s and that at 0.5 s were similar, and the damage was located at slightly left of the wheel rolling circle.

5. Conclusions

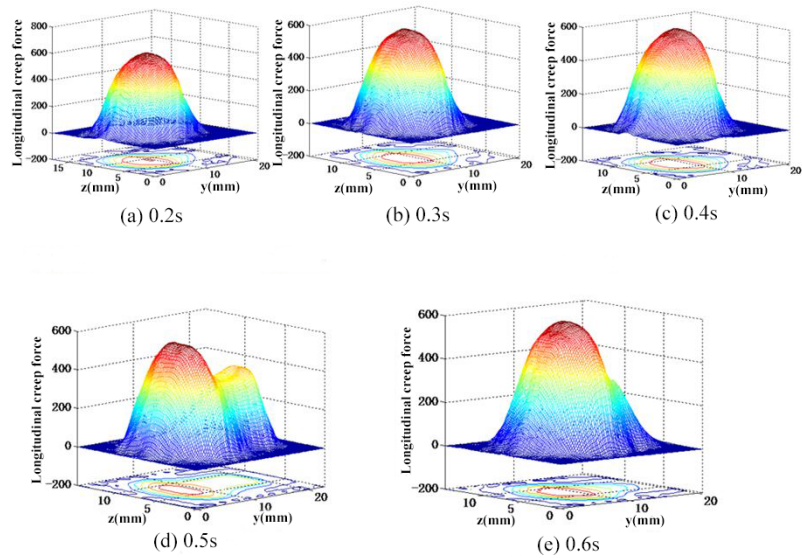A head car model of CRH2 was built with the multibody

Fig. 9. Distribution of longitudinal creep force of the wheel under different moments.
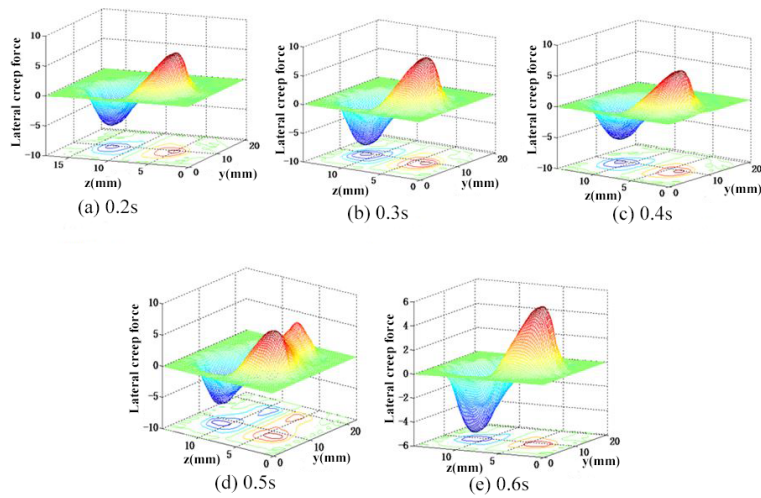

Fig. 10. Distribution of lateral creep force of the wheel under different moments.
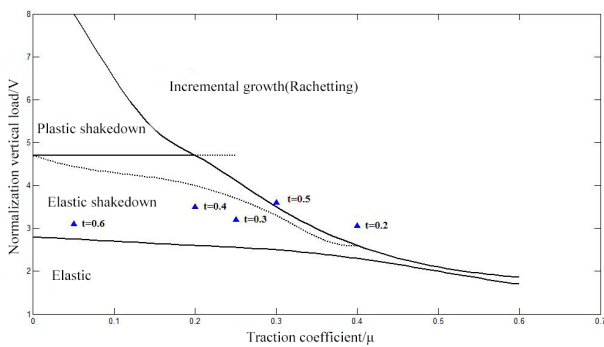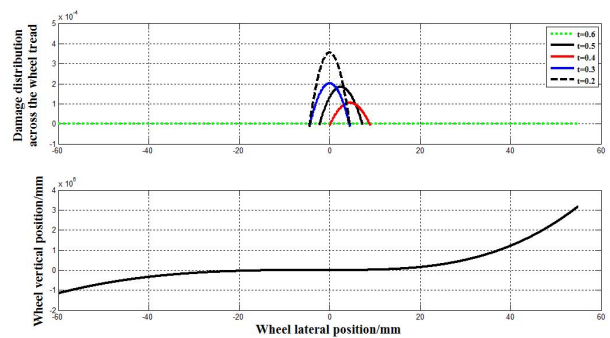

Fig. 11. Shakedown map.

Fig. 12. Distribution of wheel damage under different moments.

dynamics software UM. Dynamic contact geometric parameters of hunting movement were then obtained. With the dynamic contact geometric parameters as the initial conditions, a 3D transient elastic-plastic FEM of high-speed wheel/rail rolling contact was developed with ABAQUS. The actual geometries of the wheel tread and rail head, as well as the elastic-plastic properties, were considered in this model. This consideration made the model highly suitable for solving 3D transient rolling contact. Eventually, the normal force, creep force, and contact area in the contact patch were solved and used in the fatigue model.

The main conclusions are as follows.

After the dynamic model was built, the curves of the wheel/rail force, lateral displacement, attack angle, and velocity of the left wheel that vary with time were obtained. The varying value of lateral displacement ranged from 0 mm to 0.005 mm, and the value of the attack angle ranged from 0 rad to 0.0015 rad. The proportion of wheel/rail force, whose value was between 20000 and 80000 N, was larger than 90 %.

The longitudinal creep force at 0.2 s was significantly large because of the large normal force. However, the normal force and lateral displacement at 0.3 s, as well as the value of the longitudinal creep force, were relatively small. Contrary to that at 0.3 s, the large attack angle at 0.2 s led to a large lateral creep force. The distributions of the longitudinal and lateral creep force were almost consistent, except for that at 0.5 s. The contact area was the largest at 0.5 s because of the emergence of a main contact area and a secondary contact area within the contact patch resulting from the large lateral displacement. As a result of the large lateral displacement and the change in contact position, two peaks and two valleys of lateral creep force appeared in different regions at 0.5 s.

At 0.5 and 0.2 s, the longitudinal and lateral creep force were significantly large; hence, they were prone to RCF. However, at 0.3, 0.4 and 0.6 s, the wheel reached elastic stability, which is a relatively safe state. No damage was observed at 0.6 s. The damage at 0.2 s was located at slightly left of the wheel rolling circle because of the existence of wheel hunting movement.

Acknowledgment

References

[1] D. Tiesong, L. Wei, W. Zefeng and J. Xuesong, Prediction on rolling contact fatigue crack initiation life of rails, *Lubrication Engineering*, 38 (8) (2013) 46-51.

[2] C. Shihao et al., Research of the differences between Hertz theory and finite element method to analyze the fatigue of wheel/rail contact, *Journal of Mechanical Engineering*, 51 (6) (2015) 126.

[3] M. Taraf et al., Numerical analysis for predicting the rolling contact fatigue crack initiation in a railway wheel steel, *Engineering Fracture Mechanics*, 43 (3) (2010) 585-593.

[4] D. H. Lee, J. W. Seo and S. J. Kwon, Numerical analysis of the effect of slip ratio on the fatigue crack initiation life in rolling contact, *Advanced Materials Research*, 891-892 (2014) 1791-1796.

[5] D. Junjun, Z. Liangwei and L. Fu, Research on rail rolling contact fatigue based on the damage function, *Journal of China Railway Society*, 33 (1) (2011) 19-24.

[6] C. Chongyi, A study on wheel/rail rolling contact theory based on finite element method and it's applying, *Scientific Research on Chinese Railways* (2010).

[7] X. Zhao and Z. Li, The solution of frictional wheel-rail rolling contact with a 3D transient finite element model: Validation and error analysis, *Wear*, 271 (1) (2011) 444-452.

[8] M. Pletz, W. Daves and H. Ossberger, A wheel set/crossing model regarding impact, sliding and deformation—Explicit finite element approach, *Wear*, s 294-295 (2012) 446-456.

[9] N. Nakano and Y. Terumichi, Numerical analysis for coupled train considering 3D wheel/rail contact geometry, *Journal of Mechanical Science and Technology*, 29 (7) (2015) 2677-2683.

[10] X. Zhao, 3D transient finite element model for high-speed wheel/rail rolling contact and its application, *Journal of Mechanical Engineering*, 49 (18) (2013) 1-7.

[11] Z. Wen, L. Wu, W. Li, X. Jin and M. Zhu, Three-dimensional elastic-plastic stress analysis of wheel-rail rolling contact, *Wear*, 271 (1-2) (2011) 426-436.

[12] K. D. Vo, A. K. Tieu, H. T. Zhu and P. B. Kosasih, A 3D dynamic model to investigate wheel-rail contact under high and low adhesion, *International Journal of Mechanical Sciences*, 85 (2014) 63-75.

[13] J. F. Brunel, E. Charkaluk, P. Dufrénoy and F. Demilly, Rolling contact fatigue of railways wheels: Influence of steel grade and sliding conditions, *Procedia Engineering*, 2 (1) (2010) 2161-2169.

[14] B. Dirks and R. Enblom, Prediction model for wheel profile wear and rolling contact fatigue, *Wear*, 271 (1-2) (2011) 210-217.

[15] S. Hossein Nia, C. Casanueva and S. Stichel, Prediction of RCF and wear evolution of iron-ore locomotive wheels, *Wear*, 338-339 (2015) 62-72.

[16] A. Bevan, P. Molyneux-Berry, B. Eickhoff and M. Burstow, Development and validation of a wheel wear and rolling contact fatigue damage model, *Wear*, 307 (1-2) (2013) 100-111.

[17] J. Tunna, J. Sinclair and J. Perez, *The development of wheel wear and rolling contact fatigue model -RSSB Report for Task T549*, Rail Safety and Standards Board (2007).

[18] People's Republic of China Ministry of railways, *Trains 2008 No.28 High speed EMU Test Specification*, Beijing: General Office of the Ministry of railways (2008).

[19] Y. Jizhong, *Aerodynamic effect on running safety and sta-*

bility of high-speed train, Southwest Jiaotong University (2010).

[20] L. Guofang, Y. Yongming and D. Wangcai, Modeling and simulation analysis of vehicle-track coupling dynamics, *Journal of Lanzhou Jiaotong University*, 35 (1) (2016) 142-146.

[21] X. Qian, X. Hongxia and Z. Hai, Creep characteristics of high-speed wheel-rail steady-state rolling contact under different attack angles, *China Railway Science*, 35 (1) (2014) 606-666.

Q. Xiao received his bachelor and master degrees in mechanical engineering from East China Jiaotong University in 2001 and 2005, respectively. He received his Ph.D. degree in vehicle operation engineering from China Academy of Railway Sciences in 2012. His research interests include wheel-rail interaction of high-speed trains, computer-aided design, and computer-aided engineering.